

Research Paper

ASKAP reveals giant radio halos in two merging SPT galaxy clusters

Amanda G. Wilber^{1,2} , Melanie Johnston-Hollitt¹, Stefan W. Duchesne¹ , Cyril Tasse³, Hiroki Akamatsu⁴,
Huib Intema¹  and Torrance Hodgson¹

¹International Centre for Radio Astronomy Research (ICRAR), Curtin University, Bentley, WA 6102, Australia, ²Hamburger Sternwarte, Universität Hamburg, Gojenbergsweg 112, 21029 Hamburg, Germany, ³GEPi, Observatoire de Paris, Université PSL, CNRS, 5 Place Jules Janssen, 92190 Meudon, France and ⁴SRON Netherlands Institute for Space Research, Utrecht, The Netherlands

Abstract

Early science observations from the Australian Square Kilometre Array Pathfinder (ASKAP) have revealed clear signals of diffuse radio emission associated with two clusters detected by the South Pole Telescope via their Sunyaev Zel'dovich signal: SPT CLJ0553-3342 (MACS J0553.4-3342) and SPT CLJ0638-5358 (Abell S0592) are both high-mass lensing clusters that have undergone major mergers. To create science-fidelity images of the galaxy clusters, we performed direction-dependent (DD) calibration and imaging on these ASKAP early science observations using state-of-the-art software *killMS* and *DDFacet*. Here, we present our DD calibrated ASKAP radio images of both clusters showing unambiguous giant radio halos with largest linear scales of ~ 1 Mpc. The halo in MACS J0553.4-3342 was previously detected with Giant Metrewave Radio Telescope observations at 323 MHz but appears more extended in our ASKAP image. Although there is a shock detected in the thermal X-ray emission of this cluster, we find that the particle number density in the shocked region is too low to allow for the generation of a radio shock. The radio halo in Abell S0592 is a new discovery, and the Southwest border of the halo coincides with a shock detected in X-rays. We discuss the origins of these halos considering both the hadronic and turbulent re-acceleration models and sources of *seed* electrons. This work gives a positive indication of the potential of ASKAP's Evolutionary Map of the Universe survey in detecting intracluster medium radio sources.

Keywords: galaxies: clusters: general – galaxies: clusters: individual – galaxies: clusters: intracluster medium – radio continuum: galaxies – techniques: interferometric

(Received 1 June 2020; revised 14 August 2020; accepted 15 August 2020)

1. Introduction

Galaxy clusters are megaparsec-sized systems that contain hundreds of individual galaxies which reside within a hot pool of ionised, magnetised gas. While some resident galaxies are typically observed to emit radio emission from their active galactic nuclei (AGN), very extended and diffuse radio sources originating from the intracluster medium (ICM) have been identified in a growing number of galaxy clusters over the last several decades (see van Weeren et al. 2019, for a recent review). Theoretical and observational evidence support the suggestion that diffuse radio sources associated with the ICM are generated from the collisions, or mergers, of multiple galaxy clusters (e.g. Buote 2001; Cassano et al. 2010). As dictated by the evolution of large-scale structure in the Universe, a cluster–cluster merger occurs on a timescale of about 1 Gyr (Sarazin 2002), and during this time shock waves and turbulence are magnetically driven throughout the system. Turbulence and shocks can excite—and re-excite—relativistic electrons within the cluster magnetic field, leading to observable synchrotron

emission at radio frequencies (e.g. Brunetti & Jones 2014; Brunetti et al. 2008; Brüggén et al. 2012; Brüggén & Vazza 2015).

Merger-induced synchrotron sources can come in various forms (see Kempner et al. 2004, for a taxonomy). Some merging clusters host diffuse emission, known as *giant radio halos*, which fill the inner volume of the ICM. Other clusters show large, elongated structures on the outer edges of the ICM, called *gischt-type radio relics* or *radio shocks*. There are also cases where extended emission from resident radio galaxies is observed to be shock compressed or re-energised by a merger event of the host cluster. This type of emission does not always fit into a specific classification, but examples include the radio phoenixes in A13, A85, A133, and A4038 (Slee et al. 2001), the gently re-energised tail (GReET) in Abell 1033 (de Gasperin et al. 2017), the re-brightened tail in Abell 1132 (Wilber et al. 2018a), and the revived fossil plasma source found in Abell 1314 (Wilber et al. 2019, van Weeren et al., in preparation).

Radio halos are widely considered to be the result of turbulent re-acceleration of mildly relativistic electrons in the ICM (e.g. Brunetti et al. 2001; Donnert et al. 2013; Pinzke, Oh, & Pfrommer 2017). However, theory indicates that there should also be a population of secondary radio-emitting CRE produced from collisions between thermal protons and cosmic-ray protons in the ICM (hadronic model; Dennison 1980). It is still unknown as to how

Author for correspondence: Amanda G. Wilber, E-mail: amanda.wilber@curtin.edu.au
Cite this article: Wilber AG, Johnston-Hollitt M, Duchesne SW, Tasse C, Akamatsu H, Intema H and Hodgson T. (2020) ASKAP reveals giant radio halos in two merging SPT galaxy clusters. *Publications of the Astronomical Society of Australia* 37, e040, 1–12. <https://doi.org/10.1017/pasa.2020.34>

much of a role these secondary CRe play in generating radio halos since the expected gamma-ray contribution from these proton–proton collisions has yet to be detected in a single galaxy cluster (e.g. Ackermann *et al.* 2010, 2014; Prokhorov & Churazov 2014).

Gischt-type relics, or radio shocks, are often found to trace bow shocks occurring on the largest scales and are therefore thought to be connected to diffusive shock acceleration that operates at a shock front (Blandford & Ostriker 1978; Ensslin *et al.* 1998). X-ray observations of merging clusters typically show an overall disturbed morphology in their thermal gas; however, shock-heated gas can be identified by a sharp discontinuity in surface brightness (SB) and a corresponding jump from higher temperature to lower temperature for post-shock and pre-shock regions, respectively. To add to the challenge of their interpretation, not all merging clusters show evidence of shocks and not all detected shocks in merging clusters have radio counterparts (e.g. Botteon, Gastaldello, & Brunetti 2018; Wilber *et al.* 2018b).

The details of the necessary acceleration mechanisms and the efficiencies of low Mach number shocks are still under scientific scrutiny (see Botteon *et al.* 2020, for a recent study). Fermi-II acceleration prompted by merger turbulence and Fermi-I acceleration prompted by merger shocks are both usually too weak to accelerate electrons from thermal to ultra-relativistic energies (Botteon *et al.* 2016; Eckert *et al.* 2016; Kang, Ryu, & Jones 2012; Markevitch *et al.* 2005; Petrosian & East 2008; van Weeren *et al.* 2016b). Hence, some form of pre-acceleration or a population of relativistic *seed* electrons is required to explain cluster-scale halos and relics. While primordial accretion shocks are suspected to account for a portion of the CRe population in clusters, AGN are another viable source for seed electrons. Several examples have been found where extended radio galaxies appear to be feeding into diffuse cluster sources: for example, the remnant radio galaxy supplying seeds for the relic in the Bullet cluster 1E 0657–55.8 (Shimwell *et al.* 2015), the connection between a head-tail radio galaxy and relic in Abell 3411–3412 (Johnston-Hollitt 2017; van Weeren *et al.* 2017), and the connection between the giant radio galaxy and the ultra-steep halo in Abell 1132 (Wilber *et al.* 2018a).

The origins of cluster magnetic fields are predicted to come from a constant primordial field that has been amplified over time (see Donnert *et al.* 2018; Grasso & Rubinstein 2001, for reviews). Recent investigations of the evolution of magnetic fields in merging galaxy clusters—through high-resolution cosmological magnetohydrodynamical simulations—have revealed that although major mergers can shift the peak magnetic spectra to small scales (via small-scale dynamo) in about 1 Gyr, continuous minor mergers are necessary for steady magnetic field growth over several Gyrs (Domínguez-Fernández *et al.* 2019). Using the cryogenic X-ray microcalorimeter, soft X-ray spectrometer (Kelley *et al.* 2016), the Hitomi Collaboration *et al.* (2016) measured turbulent velocities in the Perseus cluster and found that the ICM was fairly quiescent, contradicting expectations. Synthesised observations (e.g. Roncarelli *et al.* 2018) of the not-yet-launched *Athena* X-ray satellite show that the X-ray Integral Field Unit spectrometer will have both unprecedented spectral resolution (2.5 eV at 7 keV) and spatial resolution (\sim few kpc) in measuring turbulence, even out to the cluster outskirts (see Simionescu *et al.* 2019, for a recent review).

An ongoing project for the galaxy cluster science community is to gather sufficient data on a large number of ICM sources to allow for more thorough statistical studies of clusters. The Giant

Metrewave Radio Telescope (GMRT) radio halo survey (Venturi *et al.* 2008) and extended GMRT radio halo survey (Kale *et al.* 2013) started this pursuit, providing observations of more than 60 galaxy clusters and finding radio halos in about \sim 23% of clusters. The LOFAR Two Metre Sky Survey (LoTSS; Shimwell *et al.* 2017) is currently in progress to cover the entire northern hemisphere with very high sensitivity ($100 \mu\text{Jy beam}^{-1}$) at 140 MHz. Van Weeren *et al.* (in preparation) present observations of more than 50 clusters covered in a 400 square degree region of LoTSS, listing all candidates for newly discovered diffuse cluster emission. In the southern hemisphere, Johnston-Hollitt *et al.* (in preparation) are using the GaLactic and Extra-galactic All-sky Murchison Widefield Array (MWA) survey (GLEAM; Wayth *et al.* 2015) to search for and identify candidate diffuse emission in 1 167 MCXC galaxy clusters (Meta-Catalogue of X-ray detected Clusters; Piffaretti *et al.* 2011). Clusters selected from the South Pole Telescope (SPT) catalogue, which has detected over 1 000 clusters via the Sunyaev Ze’ldovich (SZ) effect since 2015 (Bleem *et al.* 2015; Bocquet *et al.* 2019a; Bleem *et al.* 2019), will be covered by the future surveys of the Square Kilometre Array (Dewdney *et al.* 2009).

The Australian Square Kilometre Array Pathfinder (ASKAP; Johnston *et al.* 2007, 2008) is a newly commissioned radio telescope array consisting of 36 separate 12-m parabolic dish antennas operating between 700 and 1800 MHz in Western Australia. ASKAP stands apart from its predecessors due to its highly innovative Phased Array Feeds (PAFs) installed on each antenna. The PAFs are designed as a dual-polarisation chequerboard grid consisting of 188 element sensors that are cross-correlated to form 36 separate beams on the sky (Hotan *et al.* 2014; McConnell *et al.* 2016). This technology gives the telescope a large field of view ideal for rapid survey imaging (DeBoer *et al.* 2009). The Evolutionary Map of the Universe (EMU; Norris *et al.* 2011) survey will record the radio continuum over the whole Southern sky and up to $+30^\circ$ declination. Science goals of the EMU collaboration include tracing the evolution of galaxies and black holes, and further constraining cosmological parameters based on observations of large-scale structure. EMU, in conjunction with ASKAP’s Polarisation Sky Survey POSSUM (Gaensler *et al.* 2010), will uncover more details on cosmic magnetism. Predictions have been made that the ASKAP EMU survey will detect more than 100 new radio halos (Cassano *et al.* 2012), and recent work has shown that ASKAP has superb diffuse source sensitivity to emission over megaparsec (Mpc) scales (Hodgson *et al.* 2020). An EMU Pilot Survey was carried out in 2019 for a total of 10 fields and was made publicly accessible in the form of \sim 30 square degree mosaic images and calibrated visibilities in the CSIRO ASKAP Science Data Archive (CASDA; Chapman *et al.* 2017).

In this paper, we report on radio emission associated with two galaxy clusters that have been covered by ASKAP’s early science observations outside of the EMU Pilot Survey. These galaxy clusters are high-mass, merging clusters that have been detected by the SPT through their SZ signal: SPT CLJ0553–3342 (also known as MACSJ0553.4–3342; hereafter MACSJ0553) and SPT CLJ0638–5358 (also known as Abell S0592; hereafter AS0592). Due to their high-mass, both of these clusters are gravitational lenses and have been imaged with the *Hubble Space Telescope* (HST) Advanced Camera for Surveys^a (ACS; Ford *et al.* 1998). The publicly avail-

^aMACSJ0553 was imaged in band F435W, F606W, and F814W, while AS0592 was only imaged in band F606W.

Table 1. Cluster properties from SPT and Planck catalogues and Chandra observations. See Sections 1.1 and 1.2 for references.

Cluster	R.A., Dec.	SPT M_{500}	Planck M_{500}	z	L_X	T
		[$10^{14} M_\odot$]	[$10^{14} M_\odot$]		[10^{44} ergs sec $^{-1}$]	[keV]
AS0592	06 ^h 38 ^m 47.4 ^s , −53°58′29.6′	11.29 ^{+1.36} _{−1.10}	6.83 ^{+0.34} _{−0.31}	0.226	11.2 ± 0.6	9.45 ± 0.95
MACSJ0553	05 ^h 53 ^m 24.3 ^s , −33°42′43.4′	11.33 ^{+1.37} _{−1.16}	9.39 ^{+0.56} _{−0.58}	0.412	10.3 ± 0.3	12.08 ± 0.63

able ASKAP images covering these clusters show clear signs of diffuse emission present in both intracluster media. See Table 1 for quantitative details on both clusters.

In the following subsections, we outline prior scientific results found in the literature on both clusters. In Section 2, we describe the procedure we developed to carry out direction-dependent (DD) calibration and imaging on ASKAP data, as well as the data analysis methods we used to measure the properties of the diffuse emission from ASKAP in conjunction with supplementary data from other telescopes. Our findings are presented in Section 3 and we end with a discussion and conclusion in Sections 4 and 5. Throughout this paper, we assume a Λ CDM cosmology with $H_0 = 70 \text{ km s}^{-1} \text{ Mpc}^{-1}$, $\Omega_m = 0.3$, and $\Omega_\Lambda = 0.7$. All images are in the J2000 coordinate system.

1.1. MACS J0553.4-3342

MACSJ0553, also classified as SPT CLJ0553-3342, was first discovered in the Massive Cluster Survey (MACS; Ebeling, Edge, & Henry 2001). It is a massive, dynamically disturbed merging cluster, at a redshift of $z = 0.407$ (Cavagnolo et al. 2008), and has been extensively researched at optical and X-ray wavelengths. Mann & Ebeling (2012) performed a joint X-ray-optical analysis and suggested that the two X-ray peaks visible in Chandra observations represent a binary head-on merger of two similar mass clusters with a merging axis in the plane of the sky. They also assessed that the merger evolutionary stage is likely after core passage. A further, more detailed study of this system was published in Ebeling, Qi, & Richard (2017) where the dynamics of dark and luminous matter were considered. There they combined *HST* and Chandra data and found that the merger axis is actually not in the plane of the sky but at a large inclination angle, and that the less massive Western component was fully stripped by ram-pressure as it passed through the more massive Eastern subcluster.

Using a Chandra observation with longer exposure, Pandge et al. (2017) measured and mapped discontinuities in SB and temperature throughout the system and found evidence of two edges corresponding to one cold front and one shock on the Eastern side of the cluster. They report that the merger-driven cold front is behind the shock, following the morphology of other similarly merging clusters such as the *Bullet* (Markevitch et al. 2002) and *Toothbrush* (van Weeren et al. 2009) clusters. They calculated the shock Mach number to be $1.33 < \mathcal{M} < 1.72$. Both Pandge et al. (2017) and Ebeling et al. (2017) confirmed the presence of this cold front and shock and used *HST* data to surmise that there are two subclusters of galaxies that make up this system, SC1 and SC2, which are separated by a projected distance of 650 kpc. More recently, Botteon et al. (2018) used an edge detection filter and spectral analysis to search for shocks and cold fronts in a sample of 15 mass-selected clusters, including MACSJ0553, and they found that the cluster additionally hosts another cold front on the opposite, Western side of its ICM.

The most recent mass estimate of this cluster is $M_{500} = 11.33^{+1.37}_{-1.16} \times 10^{14} M_\odot$ from the SPTpol Extended Cluster Survey catalog (Bleem et al. 2019). However, the mass estimated from the *Planck* satellite is lower: $M_{500} = 9.39^{+0.56}_{-0.58} \times 10^{14} M_\odot$ (PZS1; Planck Collaboration et al. 2015). From the calculations of Pandge et al. (2017), MACSJ0553 is one of the hottest and most luminous galaxy clusters known ($T = 12.08 \pm 0.63 \text{ keV}$ and $L_{500,[0.1-2.4 \text{ keV}]} = (10.2 \pm 0.3) \times 10^{44} \text{ erg s}^{-1}$).

Bonafede et al. (2012) carried out a radio study of four massive clusters at redshifts $z > 0.3$ with GMRT observations at 323 MHz and found an extended radio halo in MACSJ0553. While two other clusters in their sample showed clear double radio relics, there were no such radio shock structures observed in MACSJ0553. They elaborated upon the unexpected absence of radio relics in this cluster, predicting that the merger axis may not be in the plane of the sky (which was later confirmed by Ebeling et al. 2017) and therefore it may be difficult to see radio shocks due to the combination of projection effects and the brightness of the halo.

1.2. Abell S0592

AS0592, also classified as SPT CLJ0638-5358 and RXC J0638.7-5358 (from the REXCESS survey; Böhringer et al. 2007), is a massive cluster with a recent mass estimate of $M_{500} = 11.29^{+1.36}_{-1.10} \times 10^{14} M_\odot$ from the SPT-SZ 2500 deg 2 catalogue (Bocquet et al. 2019b). A previous estimate of the cluster mass, from the *Planck* catalogue, is much lower: $M_{500} = 6.83^{+0.34}_{-0.31} \times 10^{14} M_\odot$ (PSZ2; Planck Collaboration et al. 2016). This cluster was covered by the ROSAT REFLEX Survey, from which the redshift was estimated to be $z = 0.221$ (De Grandi et al. 1999). An update to the redshift was provided by Piffaretti et al. (2011) where they found $z = 0.226$. An X-ray analysis for this cluster was published in Mantz (2009) where the following values were measured from a ACIS-I VFaint 19.9 ks follow-up Chandra observation: $kT = 9.5 \pm 1.0 \text{ keV}$, $L_X = (11.2 \pm 0.6) \times 10^{44} \text{ ergs sec}^{-1}$, and $M_{500} = (10.3 \pm 1.4) \times 10^{14} M_\odot$.

Although it has a lower temperature and a slightly lower mass (according to the SPT measurement), AS0592 is more X-ray luminous than MACSJ0553. In a proposal for deep XMM-Newton observations, Hughes (2009) suggested that archival Chandra and *HST* data reveal that AS0592 is undergoing a major merger. In a study of the cool-core state of *Planck*-selected clusters, Rossetti et al. (2017) used X-ray observations of AS0592 to measure the concentration parameter as defined by Santos et al. (2008). They found that the cluster has a significant SB peak but an overall disturbed X-ray morphology, and they list it as a ‘disturbed cool-core’. Botteon et al. (2018) combined four separate Chandra observations of AS0592 (for a total net exposure time of 98 ks) and noted the presence of two low-temperature, low-entropy cool-cores surrounded by a hot, disturbed ICM. They also claim that there is a shock along the Southwest edge of the ICM with a Mach number $1.61 < \mathcal{M} < 1.72$.

So far, there have been no in-depth radio studies published for this cluster, but since the X-ray studies prove it to be dynamically disturbed and hosting a shock, it is a good candidate for exhibiting diffuse intracluster emission.

2. Methods

2.1. ASKAP observations and pre-processing

Data for both clusters were obtained from CASDA (Chapman et al. 2017) and come from ASKAP's early science observations Scheduling Block (SB) 8275 and SB9596 for AS0592 and MACSJ0553, respectively. SB8275 is part of the ASKAP Early Science Broadband Survey (Project: AS034, PI: Harvey-Smith) and SB9596 is part of the ASKAP Pilot Survey for Gravitational Wave Counterparts (Project: AS111, PI: Murphy). Both SBs, observed with the `closepack36` beam footprint, contain 36 measurements sets corresponding to 36 separate beams observed by each of the 36 antennas. The full-width half maximum (FWHM) of a single primary beam is about $\sim 1 \text{ deg}^2$ at a wavelength of 20 cm. MACSJ0553 and AS0592 fall within the relative centre of a single beam pointing for their respective survey observations^b. Each beam measurement set in a SB has undergone direction-independent calibration as part of the ASKAP processing pipeline (ASKAPsoft; Guzman et al. 2019). For each SB observation, CASDA also provides a mosaiced image for an overall field of view of $\sim 30 \text{ deg}^2$.

In the following paragraph, we provide an unofficial summary of the ASKAPsoft processing pipeline for calibration and imaging of ASKAP's early science observations; however, we also refer the reader to CSIRO's ASKAPsoft documentation for further details. For direction-independent calibration, ASKAPsoft performs band-pass calibration using the standard calibrator PKS B1934-638, which is observed for 200 s in each beam before or after the science target. Per-beam processing includes averaging continuum data down to 1 MHz and applying a frequency-independent, phase-only self-calibration over a timescale of 60 s. All 36 beams are imaged and deconvolved independently. The primary beams are modelled as circular Gaussians with a size taken from holography observations of the true beam^c, and an average value is used for all 36 with an error of 10%. Image weighting is implemented through a Wiener pre-conditioning method which has a setting similar to Briggs robustness. As a final step, the 36 calibrated beam images are stitched together to form a linear mosaic in the image plane. CSIRO has provided these calibrated data sets as well as the mosaiced image on CASDA but states that early science observations have not been validated. In the release notes, they state that 'a common feature of early ASKAP data has been some low-level artefacts (at 1%) very close to bright sources (a few hundred mJy and above)'.

2.2. Additional DD processing

To test whether we could improve the image quality of the early science ASKAP data covering MACSJ0553 and AS0592, we carried out DD calibration and imaging on individual calibrated measurements sets taken from CASDA. We used third-generation calibration (3GC) software DDFACET (DDF) (Tasse et al. 2018)

and KILLMS (KMS) (Smirnov & Tasse 2015; Tasse 2014) and packages therein, to image, compute, and apply solutions for DD errors. This software is currently being utilised as part of the official processing pipeline for LoTSS (see Shimwell et al. 2019, for details).

To make comparisons with the ASKAPsoft mosaics and adjust our imaging settings accordingly, we calibrated and imaged all 36 beams of both SB8275 and SB9596 independently and created a mosaic in the image plane. Since our science targets fell within or near the centre of a single beam observation, we only used a single beam image, rather than the full mosaic, to produce science images of MACSJ0553 and AS0592. We note that, prior to our additional processing, antenna AK33 was flagged for the data covering MACSJ0553 and antenna AK03 was flagged for the data covering AS0592. We also note that the central frequencies of these measurement sets are different: 943 MHz for MACSJ0553 and 1013 MHz for AS0592. In calculating the Stokes parameter I (intensity), ASKAPsoft uses the convention $I = XX + YY$, where X and Y represent the instrumental polarisations; however, with DDF and KMS we assume $I = (XX + YY)/2$.

Our approach to DD calibration was to break up the field of view of each ASKAP beam into multiple directions, following the so-called 'faceting technique' (e.g. Tasse et al. 2018; van Weeren et al. 2016a). To process a single beam, we made a direction-independent image and used this as a template to tessellate the beam field of view into several facets, where each facet contains its own 'calibrator' source. The facet calibrators are then used to compute amplitude and phase solutions for each facet. We then applied each facet's calibration solutions simultaneously while imaging to create a DD image. As a final step, we applied a primary beam correction, assuming a Gaussian with a FWHM of $1.09 \lambda/D$, and multiplied the flux intensity values by two to account for the differing Stokes conventions.

Our techniques for implementing DD calibration and imaging on these early science observations have been modified and streamlined into a processing pipeline written in python. Plans to expand the pipeline and make it open source are underway. Full processing details of the pipeline will be presented in an upcoming paper (Wilber et al., in preparation). We refer the reader to Smirnov & Tasse (2015) and Tasse et al. (2018) for the details of the mathematical functions implemented by the KMS and DDF software.

Science images of the galaxy clusters were made with the DDF imager using a uv -range $> 60 \text{ m}^d$, a Briggs robust setting of -1.5 , and a restoring beam of 11 arcsec, which we found best matched the images made with ASKAPsoft. Further steps were taken to properly subtract emission from AGN within and near the clusters in order to accurately measure the diffuse emission. Subtraction methods are described in the following subsection. Additional images were made after subtraction, and those imaging parameters are described in Section 3 for each cluster. No astrometric offset was perceptible when comparing source positions in optical and radio maps at varying frequencies. To determine the error in the flux scale of our final ASKAP images, we created a model catalogue from a combined GLEAM extragalactic catalogue (GLEAM EGC; Hurley-Walker et al. 2017) and Sydney University Molonglo Sky Survey (SUMSS; Mauch et al. 2003) catalogue, and extrapolated flux densities to ASKAP frequencies. Our ASKAP maps were first

^bMACSJ0553 falls within the relative centre of Beam 14 of SB9596 and AS0592 falls within the relative centre of Beam 22 of SB8275.

^cSee the memo: Holographic Measurement of ASKAP Primary Beams.

^dBaselines shorter than 60 m were not used so that potential Galactic emission on very large scales would not be imaged.

convolved to the resolution of SUMSS (~ 45 arcsec) and then isolated, un-resolved sources were cross-matched to the GLEAM + SUMSS master catalogue. Using these models, we estimated the flux density at the ASKAP frequency and found that $S_{\text{image}}/S_{\text{model}}$ varied across our target beams from ~ 0.8 (near the edges) to ~ 1.1 (at the centre). For the area of the beam containing MACSJ0553, we found that the error on the flux was $\sim 10\%$ and for the area of the beam containing AS05922 we found the error to be $\sim 5\%$.

2.3. Subtraction of discrete sources

To accurately measure diffuse emission associated with the ICM in these clusters, we performed a subtraction of flux from sufficiently bright, compact AGN in the cluster environments. For point sources, measuring and modelling the peak flux across several sub-band images was sufficient. For more extended sources, several methods were attempted to accurately model the emission and remove the corresponding visibilities without introducing negative artefacts. When modelling sources to be subtracted, we used images with minimum baseline cuts to capture emission on scales < 250 kpc. Based on the redshifts of the galaxy clusters, this corresponded to $> 4500 \lambda$ for MACSJ0553 and $> 3000 \lambda$ for AS0592.

For MACSJ0553, prior to DD calibration and imaging, we created six sub-band images (bandwidth of 48 MHz each) with `WSClean` (Offringa et al. 2014) and measured the peak flux density of point source AGN which appeared to eclipse diffuse emission^e. We then used `SubtractModel` (Offringa et al. 2014) with a model file listing the measurements of the sources at the six different sub-band frequencies. `SubtractModel` performs a calculation of the spectral index ($S \propto \nu^\alpha$) of each source so that the flux can be removed from the visibilities across the full band and then subtracts the modelled visibilities from the data column. Once sources were subtracted, we then performed DD calibration on the modified measurement set and used the final image to measure the flux density of diffuse cluster-scale emission.

For AS0592, the AGN embedded in diffuse emission were much more extended and could not be modelled as point sources. These bright AGN were also producing slight artefacts, so we did not wish to subtract them prior to DD calibration^f. Instead, we carried out DD calibration, and then used `DDF.py` and `MakeMask.py` to create a compact-emission DD image with a customised mask covering the full extended emission from these radio galaxies. Using the `Predict` option of `DDF.py`, the CLEAN components from the compact image were placed into a model column. We then manually subtracted this model column from the data column and re-imaged again while applying the KMS solutions.

2.4. Supplementary data

2.4.1. X-ray

We re-processed archival Chandra data (Obs IDs: 5813 and 16598 for MACSJ0553 and AS0592, respectively) for both clusters to make our own X-ray images. The Chandra data were reduced with CIAO v4.10 with CALDB version 4.7.9. Periods of high background were detected with `lc clean` using the S3 chip and the energy band

^eSources eclipsing diffuse emission in MACSJ0553 had a low peak flux of $0.6 < S < 1.2$ mJy.

^fSources eclipsing diffuse emission in AS0592 had a moderate peak flux of $1 < S < 39$ mJy.

2.5–7 keV, and they were removed from the data. Since a thorough X-ray analysis of MACSJ0553 has already been published in Pandge et al. (2017), we found no reason to redo these calculations for the shock and used their values in our analysis. The X-ray analysis for AS0592 is less thorough in the available literature, so we determined whether the system is dynamically disturbed and confirmed the discontinuity found by Botteon et al. (2018).

2.4.2. Radio

We re-processed and re-imaged the GMRT 323 MHz observations of MACSJ0553 published by Bonafede et al. (2012) using the SPAM pipeline (see Intema et al. 2017, for details). We also imaged our SPAM calibrated data with Common Astronomy Software Applications (CASA; McMullin et al. 2007) tools `TCLEAN` deconvolver mode `mtmfs` with a uv range selection of $> 4500 \lambda$ to image compact emission only. Using CASA tools `ft` and `uvsb`, the models from the compact image were placed in a model column of the measurement set and subtracted from the data column. We then produced a compact-source-subtracted image using `TCLEAN` with a uv range of $> 100 \lambda$ and uniform weighting to allow for a comparison of the diffuse emission detected by ASKAP.

To identify potential point sources in the cluster, we obtained a S-band A-configuration VLA observation of MACSJ0553 with 196 min of integration time on the target field (Project Code: 17B-367), which we processed through the CASA VLA pipeline available in CASA 5.2.2. We imaged the processed data with CASA `TCLEAN` deconvolver `mtmfs`.

AS0592 was observed with the Australia Telescope Compact Array (ATCA; Frater et al. 1992) with the Compact Array Broadband Backend (Wilson et al. 2011) for ~ 250 min in the 16-cm band (Project Code: C2837). Data were accessed through the Australia Telescope Online Archive^g and initial bandpass and gain calibration was performed using the `miriad` software suite (Sault, Teuben, & Wright 1995). The observations were taken in the EW352 and 750D array configurations, which each have a minimum baseline of 31 m, corresponding to angular scales of ~ 16 arcmin at 2.1 GHz. Bandpass and absolute flux calibration was performed using the standard calibrator for ATCA cm observations, PKS B1934–638, and the phase calibrator for the observation was PKS 0647–475. The data went through RFI flagging, and the original 2 GHz bandwidth was reduced to ~ 1.8 GHz.

Due to the gap in the uv coverage between the inner and outer baselines, we employed a uv range selection of $< 10 k\lambda$ to ensure a well-behaved point-spread function. We used CASA and `WSClean` (Offringa et al. 2014) to perform two rounds of phase-only self-calibration followed by a round of phase and amplitude self-calibration. During imaging, the data were split into eight sub-bands of $\Delta\nu = 227.5$ MHz, though CLEANing was done by peak-finding on a full-bandwidth image to ensure faint point sources were deconvolved.

3. Results

3.1. MACS J0553.4-3342

In Figure 1: Left, we present our ASKAP image at 943 MHz after DD calibration, which shows an extended radio halo in MACSJ0553. There also appears to be an N-S elongated patch of radio emission to the East of the cluster centre, near the area where

^g<https://atoa.atnf.csiro.au/>

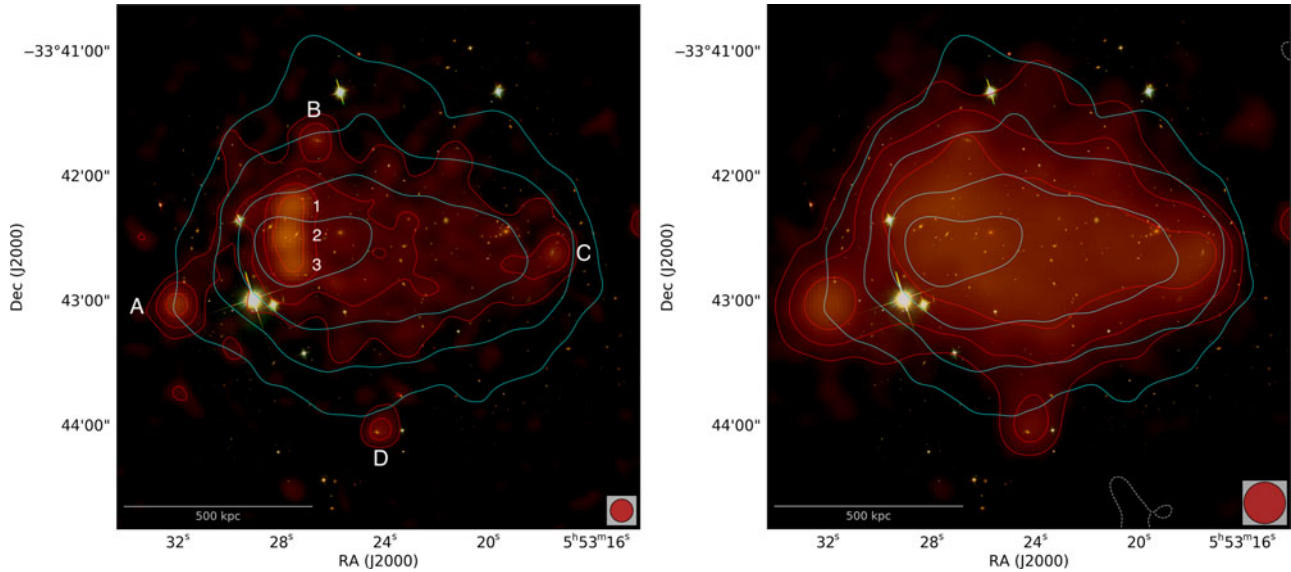


Figure 1. *HST* *i,r,g* image of MACSJ0553 with 943 MHz ASKAP radio emission and Chandra X-ray emission overlaid as contours. ASKAP emission is shown by red contours at levels $[3, 6, 12, 24] \times \sigma$. Smoothed Chandra X-ray contours are in cyan. Left: Our ASKAP image made with DDF after DD calibration ($\sigma = 20 \mu\text{Jy beam}^{-1}$, restoring beam $11 \text{ arcsec} \times 11 \text{ arcsec}$). Right: Our ASKAP image made with DDF after point source subtraction and DD calibration ($\sigma = 25 \mu\text{Jy beam}^{-1}$, restoring beam $20 \text{ arcsec} \times 20 \text{ arcsec}$). The red colour of the ASKAP emission is included for visualisation only. See text for imaging parameters.

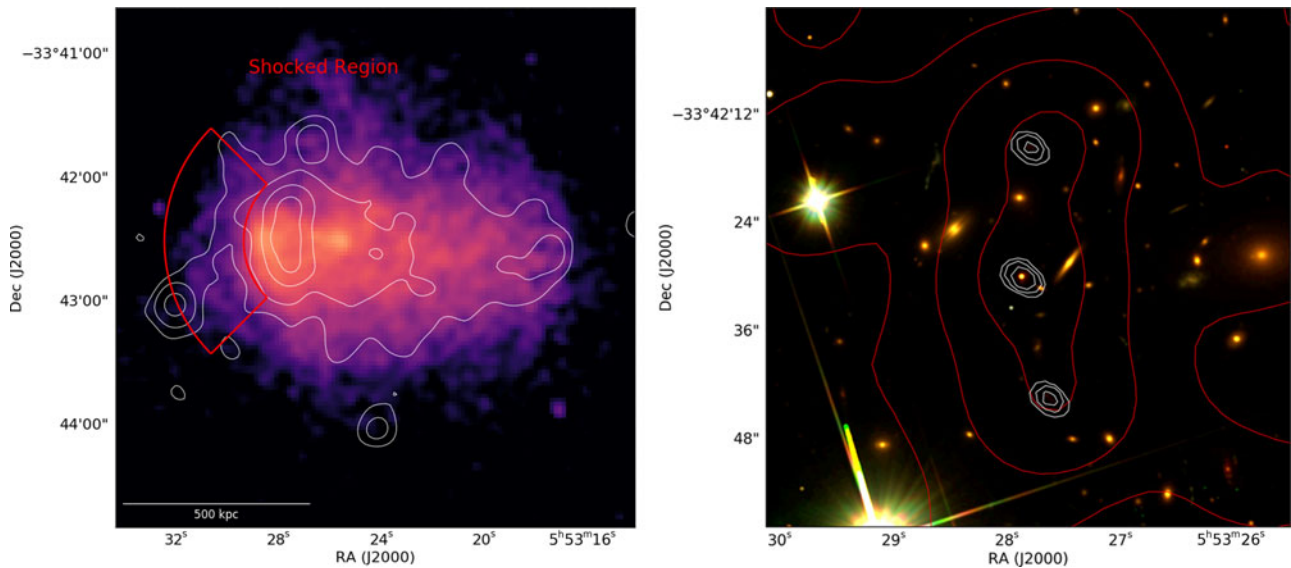


Figure 2. Left: Smoothed Chandra X-ray emission of MACSJ0553 with our ASKAP DD image overlaid as contours (levels are same as Figure 1: Left). The red region highlights the location of the shock detected in MACSJ0553 and is a reproduction from Pandge *et al.* (2017). Right: *HST* *i,r,g* image of MACSJ0553 with VLA S-band radio emission and ASKAP 943 MHz radio emission overlaid as contours. VLA emission is shown by white contours $[3, 6, 12, 24] \times \sigma$ where $\sigma = 10 \mu\text{Jy beam}^{-1}$. ASKAP emission is shown by red contours $[6, 12, 24] \times \sigma$ where $\sigma = 25 \mu\text{Jy beam}^{-1}$.

Pandge *et al.* (2017) report the presence of a shock. Although somewhat elongated, there does appear to be three individual compact components (labelled as 1, 2, and 3 in Figure 1: Left) of this structure that lie close together in an N-S orientation, as seen in projection. In our GMRT 323 MHz image (not shown), this region of emission appears much more arc-shaped^h, and it is not

^hThis is due to elongation of the beam since the GMRT is at a Northern latitude and the observation pointing is at a high Southern declination.

possible to distinguish the three cores that are partially visible in the ASKAP data. We were therefore unsure whether this emission was associated with one or more radio galaxies or if it was instead generated by a merger shock, which would make it a radio relic candidate. Although this brightened radio region does not coincide with the brightness edge seen in X-ray (see Figure 2: Left), mock radio relic simulations have shown that gischt-type relics can form within the X-ray boundary of the ICM (Nuza *et al.* 2017) or appear closer to the cluster centre depending on the viewing

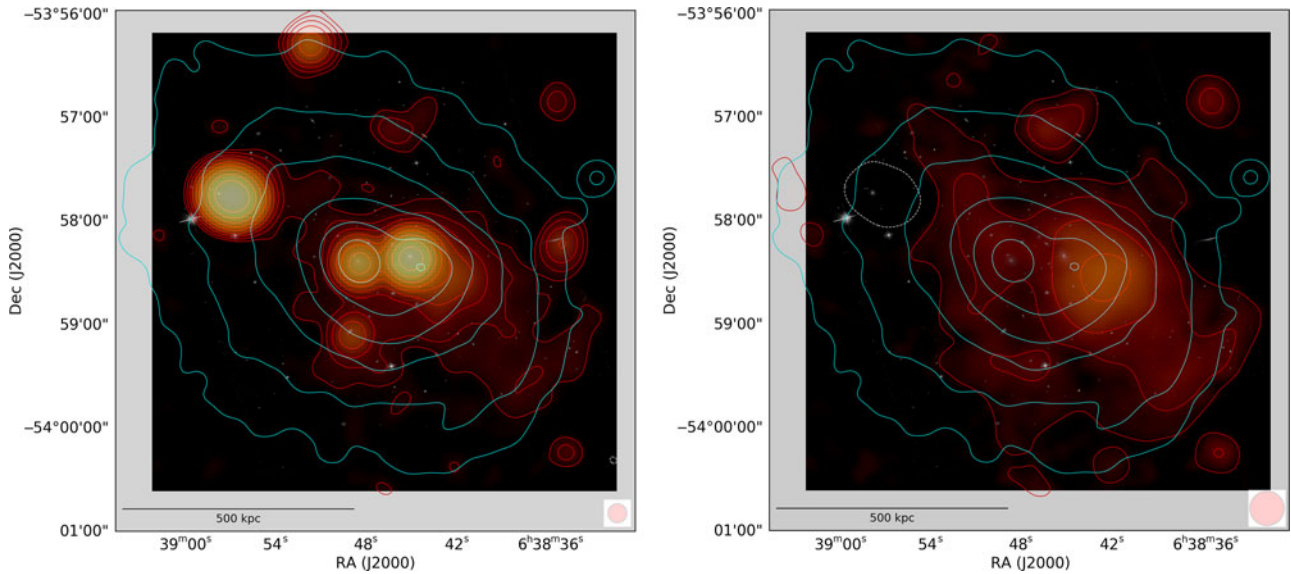


Figure 3. *HST* *r* image of AS0592 with ASKAP 1013 MHz radio emission and Chandra X-ray emission overlaid as contours. Left: our final image made with DDF ($\sigma = 20 \mu\text{Jy beam}^{-1}$, restoring beam $11 \text{ arcsec} \times 11 \text{ arcsec}$). Right: diffuse emission after subtracting compact emission imaged with a uv range $> 1 \text{ km}$ ($\sigma = 25 \mu\text{Jy beam}^{-1}$, restoring beam $20 \text{ arcsec} \times 20 \text{ arcsec}$). ASKAP emission in both images is shown by red contours at $[3, 6, 12, 24, 48, 96] \times \sigma$ and white dashed contours at $[-2] \times \sigma$. Smoothed Chandra X-ray contours are also shown in cyan. The red colour is for visualisation only. See text for imaging parameters.

angle (Skillman et al. 2013). This has been seen in a few clusters, for example, Abell 959 (Birzan et al. 2019), Abell 2255 (Akamatsu et al. 2016), and MACS J0717.5+3745 (Bonafede et al. 2009).

To confirm whether this emission was coming from one or more radio galaxies, we utilised high-resolution (configuration A) VLA S-band observations of the cluster. When overlaying our VLA image with a resolution of $2.5 \text{ arcsec} \times 1.2 \text{ arcsec}$ on the *HST* optical image, it is clear that this emission is in fact produced by either three separate compact radio galaxies or by one radio galaxy with two hotspots (see Figure 2: Right). As an estimate from the colour and size of the optical counterparts, the source in the middle (2) appears to belong to a resident galaxy of the cluster, while the Northern (1) and Southern (3) radio sources appear to be associated with faint background galaxies; however, the N and S sources could possibly be equidistant hotspots from the AGN of the middle, resident galaxy. There are no reported redshifts available for these galaxies.

To measure the integrated flux density of the radio halo in MACSJ0553, we performed a point source subtraction of the three embedded AGN. Our method for subtraction is described in Section 2.3. In the full bandwidth AKSAP image, it is apparent that there are some additional, very faint point sources around the border of the halo emission (A, B, C, and D in Figure 1: Left). Three of these very faint, compact sources (B, C, and D) appear to coincide with disk-hosting galaxies and may come from very small-scale Seyfert jets. One point source to the East (A) is beyond the edge of the *HST* optical image, so we do not know whether it belongs to a foreground or background galaxy. However, none of these faint point sources appears in any of our six sub-band images, nor in our GMRT or VLA images, and could not be measured with the AEGEAN (Hancock et al. 2012; Hancock, Trott, & Hurley-Walker 2018) source detection software, so they were not modelled or subtracted.

In Figure 1: Right, we show the radio halo emission imaged after subtracting the three N-S compact AGN (1, 2, and 3) and

subsequent DD calibration. To capture emission on larger scales, this image was made with a Briggs robust setting of -0.75 and a restoring beam of 20 arcsec . We measure the integrated flux density of the radio halo within a polygon region marked by the 3σ contour lineⁱ, where $\sigma = 25 \mu\text{Jy beam}^{-1}$. The halo has a flux density of $S_{943 \text{ MHz}} = 12.22 \pm 1.37 \text{ mJy}$ and the largest linear size (LLS) is 0.9 Mpc . The error is calculated from the estimated error on the flux scale (10%) and from the error in measuring the flux density when considering the rms noise ($\pm 0.17 \text{ mJy}$). The halo traces the X-ray emission quite well, filling the full inner volume of the cluster; however, it is slightly more elongated from East to West and shortened from North to South.

We also derive the integrated spectral index estimate of the radio halo by comparing the diffuse emission (after point source subtraction) as seen by the GMRT at 323 MHz to the diffuse emission as seen by ASKAP. To do this, we made images with uniform weighting and the same minimum uv range of 100λ , regridded the GMRT image to the ASKAP image, and smoothed both of the images to the same beam size (22 arcsec). From these images, we measure the flux density within the same region, tracing the 3σ contour line of the 943 MHz AKSAP image. We find that the radio halo has a flux density of $7.61 \pm 0.87 \text{ mJy}$ at 943 MHz and $22.02 \pm 0.92 \text{ mJy}$ at 323 MHz in these uniform-weighted images, and therefore we estimate the spectral index of the halo to be $\alpha_{323}^{943} = -0.99 \pm 0.12$.

3.2. Abell S0592

Our ASKAP image at 1013 MHz after DD calibration of AS0592 (see Figure 3: Left) shows diffuse intracluster emission that has not been previously reported in the literature. There are four bright, and somewhat extended, radio galaxies embedded in the diffuse

ⁱThe polygon is drawn such that the bordering point sources to the East and South (A and D) are not included. We assume the contribution of flux from B and C is negligible.

emission. One of these radio galaxies, at the cluster centre, has a slightly extended lobe that points toward the West. This more extended counterpart of the central radio galaxy appears to bleed into the diffuse emission in the ICM.

Our image after modelling and subtracting the bright cluster radio galaxies is shown on the right in Figure 3. To better capture diffuse emission, this image was made with a Briggs robust setting of -0.75 and a restoring beam of 20 arcsec. As explained in Sections 2.3 and 4.1, we attempted several techniques to properly subtract the radio galaxy emission in this cluster and found that the best result was to model and subtract the emission using the DDF imager after applying DD calibration solutions. The resulting image does leave a hole (negative artefact, marked by the dashed white contour line in Figure 3: Right) where the brightest radio galaxy, to the North-East, was subtracted. The diffuse intracluster emission faintly extends within this North-East region of the cluster, so we expect that our flux density measurement in this region will be an underestimation. However, the central radio galaxy with the extended Western lobe appears to leave some residual emission after subtraction, so the flux density measurement in this region will likely be an overestimation. It is difficult to quantify the amount of error that this imperfect subtraction introduces, but we assume a liberal estimate that it is on the order of $\sim 15\%$.

Due to its LLS of 1.04 Mpc, we classify this diffuse emission as a giant radio halo. From our source-subtracted DD ASKAP image, we measure the flux density of the radio halo within a region marked by the 3σ contour line where $\sigma = 25 \mu\text{Jy beam}^{-1}$. We find that the integrated flux density is $S_{1013 \text{ MHz}} = 9.95 \pm 2.16 \text{ mJy}$. The error is calculated from the estimated error on the flux scale (5%), the error in measuring the flux density when considering the rms noise ($\pm 0.18 \text{ mJy}$), and an estimate of error due to imperfect source subtraction (15%).

We were also able to image some diffuse emission in this cluster with ATCA observations. As some of the cluster radio galaxies showed small-scale extended structure in the ATCA data, we imaged the data initially using a balanced Briggs weighting with the robust parameter set to 0.0. No large-scale, diffuse emission was modelled at this stage, and the CLEAN components were subtracted before re-imaging with a natural visibility weighting. A natural weighting was required to maximise the sensitivity to the extended diffuse structure barely significant in the robust 0.0 residuals. The residuals in this naturally weighted image coincide with the radio halo detected in the ASKAP image. The residual emission after source subtraction is only significant in the full-bandwidth image centred at 2.215 GHz. The flux density of the diffuse emission measured within a region tracing the 3σ contour line, where $\sigma = 120 \mu\text{Jy beam}^{-1}$, is $S_{2215 \text{ MHz}} = 3.3 \pm 0.4 \text{ mJy}$. The error on the flux comes from a $\sim 2\%$ error due to calibration of ATCA data for the 16 cm band and the error from the rms. We are unable to quantify the error introduced from source subtraction.

We derive an integrated spectral index estimate of the radio halo in AS0592 by comparing the diffuse emission as seen by ASKAP to the diffuse emission as seen by ATCA. The spectral index estimate was calculated using measurements from our source-subtracted DD-calibrated ASKAP image and our natural-weight ATCA image. Since the spectral index should ideally be calculated from flux density measurements that are taken from images made with uniform weighting, we expect that our value will be biased, but we could not capture any diffuse emission by imaging the ATCA data with a uniform weight. The spectral index

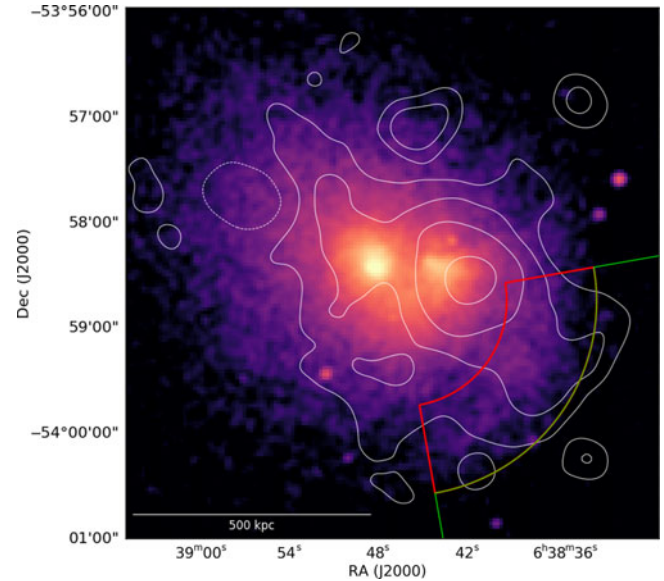


Figure 4. Smoothed Chandra X-ray emission of AS0592 with our 1013 MHz ASKAP DD image, after source subtraction, overlaid as contours (levels are same as Figure 3: Right.) Panda annulus shows where surface brightness was measured for a radial profile. The yellow curve indicates the surface brightness (SB) edge.

of the halo is estimated to be $\alpha_{1013}^{2215} = -1.41 \pm 0.25$. The error on this value comes from the error on the flux density alone, since we are unable to quantify the error due to the different weighting schemes.

In Figure 4, we present our X-ray image of AS0592 from archival Chandra data with our ASKAP DD image (after source subtraction) overlaid as contours. It is apparent that this system has two X-ray peaks with a morphology indicating a Bullet-type merger. The central peak is the brightest, and the second, dimmer peak to the West represents the ‘bullet’. The radio halo in this cluster is more offset from the X-ray gas, filling the South-Western volume of the ICM, as seen in projection, and it also follows quite closely with the central radio galaxies. The SW border of the radio halo appears to have a more linear edge, roughly coincident with the surface brightness (SB) edge reported by Botteon et al. (2018). Because they measured a steep temperature drop across this edge, Botteon et al. (2018) claim the presence of a shock. We construct a SB radial profile in a wider region¹ across the SW portion of the cluster and compare it to the profile from Botteon et al. (2018), which was measured over a narrower region. In Figure 5, the X-ray SB profiles, constructed using the *proffit* software (Eckert, Molendi, & Paltani 2011), are compared to the radio SB profile over the same region. The radio SB profile is computed by azimuthally averaging the SB in radially equal bins equivalent to the size of the synthesised beam (22 arcsec). Uncertainties in the azimuthally averaged SB are estimated via $\langle \sigma_{\text{rms}} \rangle / \sqrt{N_{\text{beam}}}$, where $\langle \sigma_{\text{rms}} \rangle$ is the mean image rms in the bin, and N_{beam} is the number of independent beams covering the bin. In Figure 5, it is apparent that the azimuthally averaged SB in radio falls off at a similar rate to the X-ray SB.

¹Region is shown as a panda annulus in Figure 4.

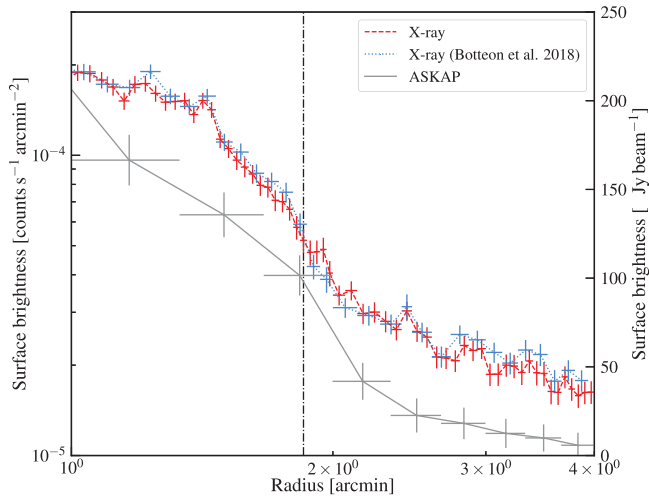


Figure 5. The azimuthally averaged SB in our radio AKSAP map is compared to the SB in X-rays. One radio SB measurement is made per beam size (22 arcsec) over 4 arcmin. The dashed vertical line marks the edge corresponding to a jump in SB. Note that radial uncertainties correspond to bin widths.

4. Discussion

4.1. Subtraction with DDF

Subtracting the bright and more extended sources in AS0592 proved to be more of a challenge than subtracting the point sources in MACSJ0553. Most methods of source subtraction involve modelling sources from a source detection software (e.g. PYBDSF (Mohan & Rafferty 2015) or AEGEAN (Hancock et al. 2018)) or from the CLEAN components of an image. The brighter AGN in AS0592 were causing slight artefacts that appeared as rings in the ASKAPsoft image. Modelling and subtracting these sources prior to DD calibration would leave those ring-type artefacts in the final image, as well as remove potential directional calibrators for this region of the sky. By modifying our DD pipeline and inserting a customised mask, we were able to make an image of the compact AGN emission only and model and subtract the CLEAN components of that image from the calibrated visibilities. We then continued to run DDF once more on the new subtracted data column, while applying the same directional calibration solutions, this time including all baselines above 60 m and including a customised mask to cover diffuse emission on the scale of the galaxy cluster. The resulting image is the remaining diffuse emission, after modelling and subtracting the compact AGN with directional calibration applied. Unfortunately, we were unable to prevent a negative artefact from occurring where the brightest radio galaxy was subtracted. We attempted to mitigate this effect by raising the CLEAN threshold on the compact image, but found that too much flux was left remaining post-subtraction.

The central radio galaxy with an extended Western lobe does appear to have emission on the same scales as the radio halo. By decreasing the minimum UV-range in the compact image, more of this extended component could be modelled and subtracted, but it was our opinion that this could possibly remove halo-related emission as well. Therefore, we only modelled and subtracted emission on scales less than 250 kpc. With only the ASKAP and ATCA observations of this cluster, it is not possible to discern how much flux in our subtracted, diffuse emission image is contributed by the central AGN. When modelling the sources

as Gaussians, measuring integrated flux densities over sub-band images, and using Subtmodel (as was done for MACSJ0553), the remaining image contained more prominent negative artefacts. Modelling the sources through the DDF imager’s Predict function yielded the best result. These methods and results proved that our DD pipeline could be easily expanded to complete more specific tasks for science-related analysis, specifically in utilising additional options available in the DDF package.

4.2. On the absence of radio relics

Although MACSJ0553 is in merging state, after core passage, and a shock and cold front have been detected in X-rays, there is no detectable radio shock emission. The absence of a radio counterpart associated with a confirmed shock has been seen in some other clusters, such as in MACS J0744.9+3927 (Wilber et al. 2018b). Following the method for calculating shock acceleration efficiency as presented in Wilber et al. (2018b) we carry out the same calculations here for the shock detected in MACSJ0553 to determine whether this shock would be able to generate a detectable radio relic.

Taking the parameters of the shock wave as measured by Pandge et al. (2017)—a Mach number of $\mathcal{M} = 1.33$ and shock velocity^k $V_{sh} = 1892 \text{ km s}^{-1}$ —and the non-detection of a radio relic, we can compute an upper limit on the particle acceleration efficiency. Comparing the dissipated kinetic power at the shock to the total power in the radio emission^l, we can estimate the acceleration efficiency using equation (2) in Botteon et al. (2016):

$$\int_{\nu_0} L(\nu) d\nu \simeq \frac{1}{2} \eta_e \Psi \rho_u V_{sh}^3 (1 - C^{-2}) \frac{B^2}{B_{cmb}^2 + B^2} S, \quad (1)$$

where η_e is the acceleration efficiency, ρ_u is the upstream density, V_{sh} is the shock velocity, C is the compression factor which is related to the Mach number via $C = 4\mathcal{M}^2/(\mathcal{M}^2 + 3)$, B is the magnetic field strength and $B_{cmb} = 3.25(1 + z)^2$, S is the surface area of the shock^m, and Ψ is the ratio of the energy injected in electrons emitting over the full spectrum versus electrons emitting in radio wavelengths, given by

$$\Psi = \frac{\int_{p_0} Q(p)E(p)dp}{\int_{p_{min}} Q(p)E(p)dp}, \quad (2)$$

where $Q(p) \propto p^{-\delta_{inj}}$ and $\delta_{inj} = 2(\mathcal{M}^2 + 1)/(\mathcal{M}^2 - 1)$ (Blandford & Eichler 1987). The momentum, p_0 , is the momentum associated with electrons that emit the characteristic frequency of the synchrotron emission, $\nu_0 = p_0^2 e B / 2\pi m_e^3 c^3$. Here, m_e is the electron mass, e its charge, and c the speed of light. We used the value from Table 5 in Pandge et al. (2017) for the upstream density in the shocked region ($\rho_u = 0.3 \times 10^{-4} \text{ cm}^{-3}$), and since the magnetic field in this cluster is not known we assume a value of $B = 1 \mu\text{G}$. For the minimum momentum in the denominator, p_{min} , we consider two cases: (1) a low value of $p_{min} = 0.1 m_e c$ representing electrons accelerated from the thermal pool, and (2) a higher value of $p_{min} = 100 m_e c$ representing a population of relativistic

^kWe determine the shock velocity by calculating the sound speed in an ideal monatomic gas using the temperature of the shocked region and the Mach number of the shock as reported in Pandge et al. (2017).

^lWe use the flux density in the pie cut region shown in Figure 2.

^mThis area is the largest linear length times the largest linear width of the shocked region, defined by the pie cut in Figure 2.3 (621 × 212 kpc²).

seed electrons. However, we find that in both cases the efficiency has to be unrealistically high, $\gg 100\%$, and we cannot infer an upper bound for η_e . This is likely due to the fact that the upstream density in the shocked region is very low. A relic is not observed, and given these acceleration efficiency calculations a relic would not be expected to form.

The clear Bullet-type merging cluster AS0592 also appears to host a shock, as measured by Botteon et al. (2018) and confirmed in our X-ray SB profile. Of the radio emission in this region, there does not appear to be any substantial brightening or structural morphology that resembles a radio relic. Instead the radio halo exhibits a linear edge roughly coincident with the location of the shock. There have been several cases where borders of radio halos are observed to coincide with, or be bounded by, SB edges detected in the thermal X-ray emission (e.g. Brown & Rudnick 2011; Markevitch et al. 2005; Shimwell et al. 2014; Vacca et al. 2014; Wang, Giacintucci, & Markevitch 2018; van Weeren et al. 2016b). Compression from the shock in this region would only be confirmed through polarisation measurements and high-resolution spectral maps. As posed by van Weeren et al. (2019), there could be turbulence after the passage of a shock, such that a previously formed radio relic now appears blended with the halo emission. We cannot compute the acceleration efficiency of the shock because it is not possible to define a region of radio emission that is potentially generated by the shock. This halo-shock connection in AS0592 is very similar to the case in Abell 520, where a Bullet-type shock front is also discovered to be coincident with the SW edge of a halo, although there the radio emission increases more sharply over the shock front from West to East (upstream to downstream) (Hoang et al. 2019).

For both clusters, the shocks detected are relatively weak. It has been proven that stronger shocks ($\mathcal{M} = 3 - 4$) are typically necessary to produce observable radio relics (Hong et al. 2014). With the results of this paper, we confirm two more cases where merger-induced shocks do not have clear radio counterparts.

4.3. On the origins of the radio halos

Although the masses estimated from SPT observations of the two clusters are relatively similar, the Planck estimated masses of these clusters differ substantially, with a larger discrepancy for AS0592: the mass estimate from SPT observations ($M_{500} = 11.29^{+1.36}_{-1.10} \times 10^{14} M_{\odot}$) is almost twice the mass estimated from Planck observations ($M_{500} = 6.83^{+0.34}_{-0.31} \times 10^{14} M_{\odot}$). In a study of mass calibration for SPT observations, Bocquet et al. (2015) found that the average cluster masses in a catalogue of 100 SPT clusters were consistently greater (by $\sim 32\%$) than their previous study (Reichardt et al. 2013), likely due to updated cosmological data. However, there are no published studies explicitly addressing discrepancies between Planck and SPT cluster masses.

In Figure 6, we plot the halos in MACSJ0553 and AS0592 by their power at 1.4 GHzⁿ versus their cluster mass as listed by both the SPT and Planck catalogues and compare them to the $P - M$ correlation reproduced from Martinez Aviles et al. (2016). In this plot, it is easy to see that although the SPT masses of the clusters are very similar, their radio powers are very different, with the halo in MACSJ0553 being much more luminous. Given the SPT

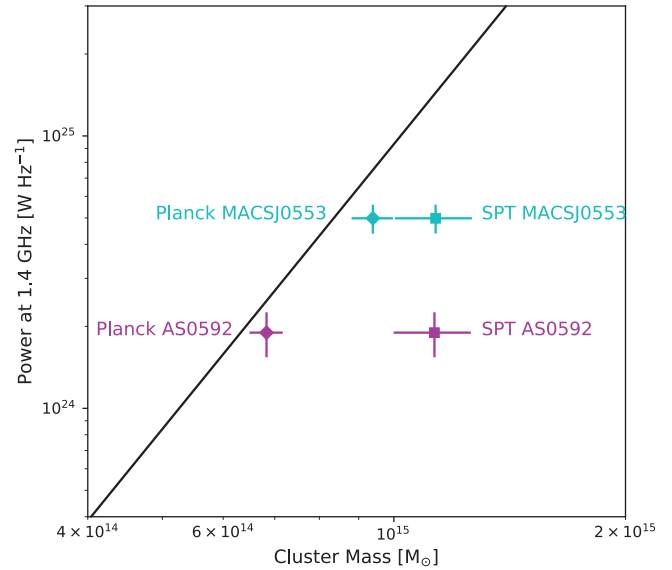


Figure 6. The powers of the halos in MACSJ0553 and AS0592 are extrapolated to 1.4 GHz and plotted against their differing mass estimates from SPT and Planck. The derived fit, or $P - M$ correlation, for a sample of halos with flux measured at 1.4 GHz is shown as a black line, from Martinez Aviles et al. (2016).

mass estimates, both of the halos also lie far outside of the current $P - M$ correlation at 1.4 GHz. If, however, one considers the Planck estimated mass, the halo powers agree more closely with the correlation that suggests that a lower mass cluster will host a lower luminosity radio halo.

In an evolutionary simulation, Donnert et al. (2013) found that the X-ray luminosity of a merging cluster will change over the lifetime of the merger, and that the power emitted by a merger-generated radio halo is transient, rising and falling along the $P - L$ correlation. This has two interesting implications: 1) because of its transience, X-ray luminosity is not an entirely reliable property for measuring cluster mass, and 2) if AS0592 and MACSJ0553 have similar masses, as indicated by the SPT-SZ measurements, the differences in the halo powers may be connected to the evolutionary state of the mergers.

As seen in our AKSAP image, the radio halo in MACSJ0553 fills the ICM and traces the X-ray emission of the cluster very well, indicating that the full volume of the ICM contains ultra-relativistic electrons. Except for the small point-source AGN coinciding with a single cluster galaxy, there does not appear to be any other radio emitting galaxies in the cluster environment. This begs the question of the origin of such a uniform population of CRE in this cluster. A calculation made by Bonafede et al. (2012) was that the timescale after core passage in MACSJ0553 would not allow sufficient time for a halo of that size to generate from turbulent re-acceleration alone. These clues lend support to the hadronic model, in which ultra-relativistic electrons can be generated by the collisions of thermal and cosmic-ray protons in the ICM. The luminosity of the halo and the flatter spectral index are also more in line with the hadronic model. It would be interesting to look at sensitive γ -ray observations of this cluster to determine whether its γ -luminosity is above the average upper limit of other clusters.

In contrast, AS0592 contains several bright radio galaxies that are injecting relativistic electrons into the surrounding environment. The radio halo in AS0592 tightly hugs the regions where the radio galaxies are present, and the central Western radio galaxy

ⁿExtrapolated to 1.4 GHz from our measured ASKAP flux densities using our spectral index estimates for each halo, and including a k -correction.

even appears to have lobe emission that bleeds into the emission of the halo. Given its morphology and proximity to the cluster radio galaxies, it is probable that the radio halo was generated from a contributed population of AGN seed, or remnant, electrons, which have then been ‘boosted’ by the turbulence of the cluster merger. We suspect that observations from the upcoming EMU survey will reveal many more examples where diffuse cluster sources are clearly fed by remnant AGN emission.

The turbulent re-acceleration model predicts that radio halos will be generated by a larger population of lower-energy electrons, yielding a steeper spectral index (Brunetti et al. 2008). Our spectral index estimate for the halo in AS0592 almost qualifies as ultra-steep (where $\alpha \leq -1.5$), but we are wary of regarding this value as accurate because it was difficult to recover the diffuse emission in this cluster with higher frequencies. We were also unable to utilise low-frequency MWA observations due to the lower resolution of the interferometer and significant source-blending, as seen in GLEAM images. High-resolution, low-frequency observations would be needed to accurately subtract the compact radio galaxies and measure the flux density of the radio halo in this cluster. Nonetheless, due to its more irregular morphology, lower luminosity, and association with nearby galaxies, we argue that the halo in AS0592 falls more in line with the turbulent re-acceleration model.

5. Conclusions

Early science survey observations from ASKAP were made public through CASDA in 2019. Examining the data, we found signs of diffuse emission associated with two high-mass, merging clusters: MACSJ0553 and AS0592. We pulled the calibrated data sets covering these clusters from CASDA and performed further processing using our own pipeline, implementing the software packages DDFACET and KILLMS (Tasse et al. 2018) to calibrate against directional errors in the data.

From our DD ASKAP images, we confirm the presence of a giant radio halo in MACSJ0553 (previously detected by Bonafede et al. 2012) and announce the discovery of a giant radio halo in AS0592. The halos have a similar LLS of ~ 1 Mpc but differ in radio luminosity despite the similar masses of the clusters. We find the flux densities of the halos to be $S_{943 \text{ MHz}} = 12.22 \pm 1.37$ mJy and $S_{1013 \text{ MHz}} = 9.95 \pm 2.16$ mJy for MACSJ0553 and AS0592, respectively. In comparing measurements at other frequencies, we estimate the integrated spectral indices to be $\alpha_{323}^{943} = -0.99 \pm 0.12$ for the halo in MACSJ0553 and $\alpha_{1013}^{2215} = -1.41 \pm 0.25$ for the halo in AS0592.

The halo in MACSJ0553 traces the thermal emission of the cluster extremely well and does not appear to be fed by seed electrons from any cluster AGN. Due to its size, morphology, high luminosity, and flatter spectral index, we argue that this halo falls more in line with the hadronic model. In contrast, the radio halo in AS0592 is more irregular in shape and does not fill the full volume of the cluster, but instead closely traces the location of resident radio galaxies. We argue that these cluster radio galaxies contribute a population of seed electrons that have been re-energised by the major merger of the cluster. Due to its morphology, lower radio luminosity, its association with radio galaxies in the cluster, and the fact that the halo is offset from the X-ray gas, we argue that this halo falls more in line with the turbulent re-acceleration model.

As indicated by their thermal X-ray emission, both clusters have independently undergone major mergers and are in the phase after core passage. Both clusters also show SB edges in their X-ray radial profiles, corresponding to shocks as confirmed by a jump in temperature. However, neither of the clusters host a radio shock. While the merger shocks have relatively low mach numbers, the upstream particle density in MACSJ0553 is too small to produce a radio shock. In AS0592, the shock boundary coincides roughly with the edge of the radio halo.

It is compelling to consider the differences in the halos for two clusters that have such similar merger dynamics, mass, and X-ray properties. This reinforces our uncertainty regarding the origin of these sources. High-resolution, low-frequency observations of these clusters will help to constrain the spectral indices of the radio halos, and, in conjunction with more sensitive γ -ray observations, may provide more clarity on their distinctive origins.

Acknowledgements. The Australian SKA Pathfinder is part of the Australia Telescope National Facility which is managed by CSIRO. Operation of ASKAP is funded by the Australian Government with support from the National Collaborative Research Infrastructure Strategy. ASKAP uses the resources of the Pawsey Supercomputing Centre. Establishment of ASKAP, the Murchison Radio-astronomy Observatory, and the Pawsey Supercomputing Centre are initiatives of the Australian Government, with support from the Government of Western Australia and the Science and Industry Endowment Fund. We acknowledge the Wajarri Yamatji people as the traditional owners of the Observatory site. This paper includes archived data obtained through the CSIRO ASKAP Science Data Archive, CASDA (<http://data.csiro.au>). The ATCA is part of the Australia Telescope National Facility which is funded by the Australian Government for operation as a National Facility managed by CSIRO. This paper includes archived data obtained through the Australia Telescope Online Archive (<http://atoa.atnf.csiro.au>). This work was supported by resources provided by the Pawsey Supercomputing Centre with funding from the Australian Government and the Government of Western Australia. We acknowledge and thank the builders of ASKAPsoft. AGW acknowledges the Hamburger Sternwarte for its computing resources. AGW thanks Aidan Hotan, Ron Ekers, Dave McConnell, Marcus Brüggen, and Andrea Botteon. SWD acknowledges an Australian Government Research Training Program scholarship administered through Curtin University. In memory of Jean-Pierre Macquart.

References

- Ackermann, M., et al. 2010, *ApJ*, **717**, L71
- Ackermann, M., et al. 2014, *ApJ*, **787**, L8
- Akamatsu, H., et al. 2016, *A&A*, **593**, L7
- Birzan, L., et al. 2019, *MNRAS*, **487**, 4775
- Blandford, R., & Eichler, D. 1987, *PhR*, **154**, 1
- Blandford, R. D., & Ostriker, J. P. 1978, *ApJ*, **221**, L29
- Bleem, L. E., et al. 2015, *ApJs*, **216**, 27
- Bleem, L. E., et al. 2019, arXiv e-prints, p. [arXiv:1910.04121](https://arxiv.org/abs/1910.04121)
- Bocquet, S., et al. 2015, *ApJ*, **799**, 214
- Bocquet, S., et al. 2019a, *ApJ*, **878**, 55
- Bocquet, S., et al. 2019b, *ApJ*, **878**, 55
- Böhringer, H., et al. 2007, *A&*, **469**, 363
- Bonafede, A., et al. 2009, *A&*, **503**, 707
- Bonafede, A., et al. 2012, *MNRAS*, **426**, 40
- Botteon, A., Gastaldello, F., Brunetti, G., & Dallacasa, D. 2016, *MNRAS*, **460**, L84
- Botteon, A., Gastaldello, F., & Brunetti, G. 2018, *MNRAS*, **476**, 5591
- Botteon, A., Brunetti, G., Ryu, D., & Roh, S. 2020, *A&A*, **634**, A64
- Brown, S., & Rudnick, L. 2011, *MNRAS*, **412**, 2
- Brüggen, M., & Vazza, F. 2015, Turbulence in the Intracluster Medium, 599, doi: [10.1007/978-3-662-44625-6_21](https://doi.org/10.1007/978-3-662-44625-6_21)
- Brüggen, M., Bykov, A., Ryu, D., & Röttgering, H. 2012, *SSRv*, **166**, 187

- Brunetti, G., & Jones, T. W., 2014, *Int. J. Mod. Phys. D*, **23**, 1430007
- Brunetti, G., Setti, G., Feretti, L., & Giovannini, G. 2001, *MNRAS*, **320**, 365
- Brunetti, G., et al. 2008, *Nature*, **455**, 944
- Buote, D. A. 2001, *ApJ*, **553**, L15
- Cassano, R., Etori, S., Giacintucci, S., Brunetti, G., Markevitch, M., Venturi, T., & Gitti, M. 2010, *ApJ*, **721**, L82
- Cassano, R., Brunetti, G., Norris, R. P., Röttgering, H. J. A., Johnston-Hollitt, M., & Trasatti, M. 2012, *A&A*, **548**, A100
- Cavagnolo, K. W., Donahue, M., Voit, G. M., & Sun, M. 2008, *ApJ*, **682**, 821
- Chapman, J. M., et al. 2017, in *Astronomical Data Analysis Software and Systems XXV*, ed. N. P. F. Lorente, K. Shorridge, & R. Wayth, *Astronomical Society of the Pacific Conference Series* (Vol. 512), 73
- De Grandi, S., et al. 1999, *ApJ*, **514**, 148
- DeBoer, D. R., et al. 2009, *IEEE Proc.*, **97**, 1507
- Dennison, B. 1980, *ApJ*, **239**, L93
- Dewdney, P. E., Hall, P. J., Schilizzi, R. T., & Lazio, T. J. L. W. 2009, *IEEE. Proc.*, **97**, 1482
- Domínguez-Fernández, P., Vazza, F., Brüggén, M., & Brunetti, G. 2019, *MNRAS*, **486**, 623
- Donnert, J., Dolag, K., Brunetti, G., & Cassano, R. 2013, *MNRAS*, **429**, 3564
- Donnert, J., Vazza, F., Brüggén, M., & ZuHone, J. 2018, *SSRv*, **214**, 122
- Ebeling, H., Edge, A. C., & Henry, J. P. 2001, *ApJ*, **553**, 668
- Ebeling, H., Qi, J., & Richard, J. 2017, *MNRAS*, **471**, 3305
- Eckert, D., Molendi, S., & Paltani, S. 2011, *A&A*, **526**, A79
- Eckert, D., et al. 2016, *MNRAS*, **461**, 1302
- Ensslin, T. A., Biermann, P. L., Klein, U., & Kohle, S. 1998, *A&A*, **332**, 395
- Ford H. C., et al. 1998, *Advanced camera for the Hubble Space Telescope*, 234–248, doi: [10.1117/12.324464](https://doi.org/10.1117/12.324464)
- Frater, R. H., Brooks, J. W., & Whiteoak, J. B. 1992, *J. Electric. Electron. Eng. Australia*, **12**, 103
- Gaensler, B. M., Landecker, T. L., & Taylor, A. R., & POSSUM Collaboration 2010, in *American Astronomical Society Meeting Abstracts #215*, 470.13
- Grasso, D., & Rubinstein, H. R. 2001, *PhR*, **348**, 163
- Guzman, J., et al. 2019, *ASKAPsoft: ASKAP science data processor software* (ascl:1912.003)
- Hancock, P. J., Murphy, T., Gaensler, B. M., Hopkins, A., & Curran, J. R. 2012, *MNRAS*, **422**, 1812
- Hancock, P. J., Trott, C. M., & Hurley-Walker, N. 2018, *PASA*, **35**, e011
- Hitomi Collaboration, et al. 2016, *Nature*, **535**, 117
- Hoang, D. N., et al. 2019, *A&A*, **622**, A20
- Hodgson, T., Johnston-Hollitt, M., McKinley, B., Vernstrom, T., & Vacca, V. 2020, *arXiv e-prints*, p. [arXiv:2007.10578](https://arxiv.org/abs/2007.10578)
- Hong, S. E., Ryu, D., Kang, H., & Cen, R. 2014, *ApJ*, **785**, 133
- Hotan, A. W., et al. 2014, *PASA*, **31**, e041
- Hughes, J. P. 2009, *XMM-Newton Observations of the Merging Cluster Abell S0592*, *XMM-Newton Proposal*
- Hurley-Walker, N., et al. 2017, *MNRAS*, **464**, 1146
- Intema, H. T., Jagannathan, P., Mooley, K. P., & Frail, D. A. 2017, *A&A*, **598**, A78
- Johnston-Hollitt, M. 2017, *NatAs*, **1**, 0014
- Johnston, S., et al. 2007, *PASA*, **24**, 174
- Johnston, S., et al. 2008, *ExA*, **22**, 151
- Kale, R., et al. 2013, *A&A*, **557**, A99
- Kang, H., Ryu, D., & Jones, T. W. 2012, *ApJ*, **756**, 97
- Kelley, R. L., et al. 2016, *The Astro-H high resolution soft X-ray spectrometer*, 99050V, doi: [10.1117/12.2232509](https://doi.org/10.1117/12.2232509)
- Kempner, J. C., Blanton, E. L., Clarke, T. E., Enÿlin, T. A., Johnston-Hollitt, M., & Rudnick, L. 2004, in *The Riddle of Cooling Flows in Galaxies and Clusters of Galaxies*, ed. T. Reiprich, J. Kempner, & N. Soker, 335 ([arXiv:astro-ph/0310263](https://arxiv.org/abs/astro-ph/0310263))
- Mann A. W., Ebeling H., 2012, *MNRAS*, **420**, 2120
- Mantz A., 2009, PhD thesis, Stanford University
- Markevitch M., et al. 2002, *ApJ*, **567**, L27
- Markevitch, M., Govoni, F., Brunetti, G., & Jerius, D. 2005, *ApJ*, **627**, 733
- Martinez Aviles, G., et al. 2016, *A&A*, **595**, A116
- Mauch T., et al. 2003, *MNRAS*, **342**, 1117
- McConnell, D., et al. 2016, *PASA*, **33**, e042
- McMullin, J. P., Waters, B., Schiebel, D., Young, W., & Golap, K. 2007, in *Astronomical Data Analysis Software and Systems XVI*, ed. R. A. Shaw, F. Hill, & D. J. Bell, *Astronomical Society of the Pacific Conference Series* (Vol. 376), 127
- Mohan, N., & Rafferty, D. 2015, *PyBDSF: Python Blob Detection and Source Finder* (ascl:1502.007)
- Norris, R. P., et al. 2011, *PASA*, **28**, 215
- Nuza, S. E., Gelszinnis, J., Hoefl, M., & Yepes, G. 2017, *MNRAS*, **470**, 240
- Offringa, A. R., et al. 2014, *MNRAS*, **444**, 606
- Pandge, M. B., et al. 2017, *MNRAS*, **472**, 2042
- Petrosian, V., & East, W. E. 2008, *ApJ*, **682**, 175ApJ, **682**, 175
- Piffaretti, R., Arnaud, M., Pratt, G. W., Pointecouteau, E., & Melin, J. B. 2011, *A&A*, **534**, A109
- Pinzke, A., Oh, S. P., & Pfrommer, C. 2017, *MNRAS*, **465**, 4800
- Planck Collaboration, et al. 2015, *A&A*, **581**, A14
- Planck Collaboration, et al. 2016, *A&A*, **594**, A27
- Prokhorov, D. A., & Churazov, E. M. 2014, *A&A*, **567**, A93
- Reichardt, C. L., et al. 2013, *ApJ*, **763**, 127
- Roncarelli, M., et al. 2018, *A&A*, **618**, A39
- Rossetti, M., Gastaldello, F., Eckert, D., Della Torre, M., Pantiri, G., Cazzoletti, P., & Molendi, S. 2017, *MNRAS*, **468**, 1917
- Santos, J. S., Rosati, P., Tozzi, P., Böhringer, H., Etori, S., & Bignamini, A. 2008, *A&A*, **483**, 35
- Sarazin, C. L. 2002, *The Physics of Cluster Mergers*, 1–38, doi: [10.1007/0-306-48096-4_1](https://doi.org/10.1007/0-306-48096-4_1)
- Sault, R. J., Teuben, P. J., & Wright, M. C. H. 1995, in *Astronomical Data Analysis Software and Systems IV*, ed. R. A. Shaw, H. E. Payne, & J. J. E. Hayes, *Astronomical Society of the Pacific Conference Series* (Vol. 77), 433 ([arXiv:astro-ph/0612759](https://arxiv.org/abs/astro-ph/0612759))
- Shimwell, T. W., Brown, S., Feain, I. J., Feretti, L., Gaensler, B. M., & Lage, C. 2014, *MNRAS*, **440**, 2901
- Shimwell, T. W., et al. 2015, *MNRAS*, **449**, 1486
- Shimwell, T. W., et al. 2017, *A&A*, **598**, A104
- Shimwell, T. W., et al. 2019, *A&A*, **622**, A1
- Simionescu, A., et al. 2019, *SSRv*, **215**, 24
- Skillman, S. W., et al. 2013, *ApJ*, **765**, 21
- Slee, O. B., Roy, A. L., Murgia, M., Andernach, H., & Ehle, M. 2001, *AJ*, **122**, 1172
- Smirnov, O. M., & Tasse, C. 2015, *MNRAS*, **449**, 2668
- Tasse, C. 2014, *A&A*, **566**, A127
- Tasse, C., et al. 2018, *A&A*, **611**, A87
- Vacca, V., Feretti, L., Giovannini, G., Govoni, F., Murgia, M., Perley, R. A., & Clarke, T. E. 2014, *A&A*, **561**, A52
- Venturi, T., Giacintucci, S., Dallacasa, D., Cassano, R., Brunetti, G., Bardelli, S., & Setti, G. 2008, *A&A*, **484**, 327
- Wang, Q. H. S., Giacintucci, S., & Markevitch, M. 2018, *ApJ*, **856**, 162
- Wayth, R. B., et al. 2015, *PASA*, **32**, e025
- Wilber, A., et al. 2018a, *MNRAS*, **473**, 3536
- Wilber, A., et al. 2018b, *MNRAS*, **476**, 3415
- Wilber, A., et al. 2019, *A&A*, **622**, A25
- Wilson, W. E., et al. 2011, *MNRAS*, **416**, 832
- de Gasperin, F., et al. 2017, *Sci. Adv.*, **3**, e1701634
- van Weeren, R. J., et al. 2009, *A&A*, **506**, 1083
- van Weeren, R. J., et al. 2016a, *ApJ*, **223**, 2
- van Weeren, R. J., et al. 2016b, *ApJ*, **818**, 204
- van Weeren, R. J., et al. 2017, *NatAs*, **1**, 0005
- van Weeren R. J., et al. 2019, *SSRv*, **215**, 16